Computational Condensed Matter 44 (2025) e01103

Contents lists available at ScienceDirect

Computational Condensed Matter

journal homepage: www.elsevier.com/locate/cocom

Optoelectronic and mechanical properties of antimony sulfide selenide ternary $Sb_2(S_xSe_{1-x})_3$ alloys using first principles methods

M. Sitaula [a], V.T. Barone [a], S.R. Kandel [a], B. K C [a], B.B. Dumre [b], R.J. Ellingson [a], S.V. Khare [a,*]

[a] Department of Physics and Astronomy, and Wright Center for Photovoltaics Innovation and Commercialization (PVIC), University of Toledo, Toledo, OH, 43606, USA
[b] University of California, Merced, CA, 95343, USA

ARTICLE INFO

Keywords:
Antimony sulfide-selenide
Density functional theory
First principles
Mechanical properties
Electronic properties
Optical properties
Vibrational properties

ABSTRACT

We have computationally studied antimony sulfide-selenide, $Sb_2(S_xSe_{1-x})_3$ ($0 \leq x \leq 1$) alloy system, using density functional theory (DFT) and beyond to explore the structural, energetic, mechanical, vibrational, and optoelectronic properties at different concentrations. We employed the Special Quasirandom Structure (SQS) approach to investigate intermediate alloy compositions, uncovering trends in alloy behavior not previously explored in DFT studies. Our lattice constants and bandgap values for the end members compare well with the available experimental data, while those for the intermediate compositions are predictive. The electronic bandgap with a tunable range of 1.1–1.8 eV was investigated. It was found to increase linearly with higher sulfur concentration. The average effective masses of electrons and holes were comparable. In addition, all members of this alloy system showed mechanical stability except for $x = 0.25$. The intermediate concentrations ($x = 0.25$, 0.50, and 0.75) all had a similar bulk modulus of $\approx$ 15 GPa. All the alloys are vibrationally stable. A high absorption coefficient with lower reflectivity within the visible light range makes this alloy system a good absorber of solar irradiation.

1. Introduction

The optimization of photovoltaic materials is central to advancing renewable energy technologies, with semiconductor alloys playing a key role in this domain. Over the last several years, antimony chalcogenides, such as antimony selenide (Sb_2Se_3), antimony sulfide (Sb_2S_3) and their alloys $Sb_2(S_xSe_{1-x})_3$ ($0 \leq x \leq 1$) have become highly promising candidates for photovoltaic applications. They possess a tunable bandgap (1.1–1.7 eV) and a high absorption coefficient ($>10^5$ cm^{-1}) in the visible light range [1–4]. Furthermore, due to their high natural abundance and non-toxic constituent elements, these compounds are considered potential alternatives to traditional thin-film solar cells such as CdTe and $Cu(In, Ga)Se_2$ [5–8].

Several experimental techniques have been developed to synthesize the antimony sulfide-selenide $Sb_2(S, Se)_3$ based solar cells, studying their optoelectronic properties and highlighting their potential for photovoltaics. Lu et al. reported the vapor transport deposition method for $Sb_2(S, Se)_3$ thin films, achieving an optimal band gap of ~1.33 eV and an efficiency of 7.03 % without a hole transport layer [9]. Sanchez et al. by optimization through vacuum thermal evaporation has led to a conversion efficiency of 5.5–6.2 % for $Sb_2S_{0.7}Se_{2.3}$ composition, emphasizing the potential of these alloys in solar energy devices [10]. Gao et al. demonstrated that pulsed laser deposition, by varying the S/(S + Se) ratio in $Sb_2(S_xSe_{1-x})_3$ compound targets, achieved tunable bandgaps of 1.31, 1.38, and 1.43 eV for $x = 0.15$, 0.25, 0.53 respectively, all close to the ideal value of the Shockley–Queisser limit [3,11]. Perez et al. through device simulation using Solar Cell Capacitance Simulator in One Dimension (SCAPS-1D) software suggested that replacing the typical CdS buffer layer with Cd-free SnS_2 in $Sb_2(S, Se)_3$ based solar cells enhances efficiency from 10.5 to 11.1 % [1]. Xio et al. reported that a novel homo-heterojunction antimony chalcogenide solar cell, optimized using wxAMPS software, achieved 26.97 % efficiency, with an open-circuit voltage (V_{OC}) of 0.885V, a short-circuit current density (J_{SC}) of 36.14 mA/cm^2, and a filling factor (FF) of 84.30 % [12]. All these methods underscore the potential of diverse synthesis techniques to enhance $Sb_2(S, Se)_3$ based solar cell efficiency.

Despite these various experimental techniques, theoretical studies on the ternary $Sb_2(S_xSe_{1-x})_3$ alloys at different concentrations of x are limited. For the end members of these $Sb_2(S_xSe_{1-x})_3$ compounds, theoretical bandgaps are close to the ideal bandgaps predicted based on the composition dependence of x [7]. However, detailed computational studies of intermediate compositions are lacking. Therefore, systematic

* Corresponding author.
E-mail address: sanjay.khare@utoledo.edu (S.V. Khare).

https://doi.org/10.1016/j.cocom.2025.e01103
Received 22 April 2025; Received in revised form 28 July 2025; Accepted 29 July 2025
Available online 5 August 2025

investigations of the $Sb_2(S_xSe_{1-x})_3$ alloys are important to advance their development.

In this work, for the $Sb_2(S_xSe_{1-x})_3$ ($0 \leq x \leq 1$) alloy system, we studied the structural, energetic, mechanical, vibrational, and optoelectronic properties using density functional theory (DFT) and beyond. The bandgap tailoring within the range of 1.1–1.8 eV was obtained, making it attractive for solar cell design. We investigated the intermediate compositions of the alloy system using the SQS approach, revealing trends in alloy behavior not explored in prior DFT studies. Our results for intermediate members of the alloy remain predictive for future endeavors. We further investigated that all members of this alloy system are vibrationally stable. Bandgaps have a linear upward trend with an increase in sulfur concentration. All members of this alloy system are mechanically stable, except for x = 0.25. A high absorption coefficient with lower reflectivity in the visible range makes this alloy system an efficacious absorber of solar irradiation. Our computational approach to this work demonstrates the potential of the alloys $Sb_2(S_xSe_{1-x})_3$ in solar cell applications.

2. Computational methods

The density functional theory (DFT) and beyond computations were conducted using the Vienna Ab initio Simulation Package (VASP) [13–18]. The Perdew-Burke-Ernzerhof (PBE) [19–21] generalized gradient approximation (GGA) exchange-correlation functional was employed in the Projector-Augmented-Wave (PAW) method [16, 22–26]. To ensure the accuracy of the calculations, the electron density was approximated by including the outer valence electrons as well as the inner semi-core s-electrons of Sb, S, and Se. A plane-wave energy cut-off of 500 eV was employed. The Brillouin zone was sampled using a (8, 3, 3) Γ-centered k-point mesh in our calculations. Each atom was structurally relaxed until the forces were reduced to less than 0.01 eV/Å. During the electronic iteration, an energy convergence criterion of 10^{-6} eV per atom was employed, utilizing a Gaussian smearing method with a width of 0.05 eV. At the beginning, initial crystal structures were obtained from the Materials Project [27]. To model the random S/Se occupation in the disordered crystal structure, SQS [28,29] models were generated using the mcsqs code implemented in the Alloy Theoretic Automated Toolkit (ATAT) [30–33]. To simulate plausible random configurations, unit cells of conventional monoclinic structure (space group: *Pm*). Were generated at concentrations of x = 0.25, 0.50, and 0.75.

During the geometry optimization of the crystal structures, atomic positions, cell shape, and cell volume were relaxed, and all structures were found to be non-magnetic. Following relaxation, high-precision static calculations were conducted to accurately determine the ground-state energies of the reactants and products, which were then used to calculate the formation energy. The formation energy per formula unit of $Sb_2(S_xSe_{1-x})_3$ is calculated as [17,34,35]:

$$\Delta E_f = E[Sb_2(S_xSe_{1-x})_3] - 2[E_{Sb}] - 3[x\,E_s + (1-x)\,E_{Se}], \quad (1)$$

where E_{Sb}, E_s and E_{Se} are the ground-state energies of antimony, sulfur and selenium (space group: R $\overline{3}$ m), (space group: $P2_1$), (space group: $P2_1/c$) respectively.

The elastic constants were calculated by employing strained supercells, where the Hessian matrices of the directional second derivatives of energy with respect to cell distortions were computed using finite difference methods [36]. For each structure, the average bulk modulus (B) and shear modulus (G) were determined from the elastic tensor (C_{ij}) using the Voigt-Reuss-Hill averaging method [37–42]. Pugh's ratio and Vickers hardness were calculated following the approaches outlined by Pugh [41,43–45], and Tian et al. [34,46–49] as:

$$k = G/B \text{ and } H_V = 0.92k^{1.137}G^{0.708}, \text{respectively.} \quad (2)$$

The mechanical stability of each structure in the orthorhombic crystal system was evaluated by ensuring the positive definiteness of elastic constants C_{ij}, in accordance with the established mechanical stability criterion [41,50,51] as:

$$\begin{aligned} &C_{11} > 0, C_{22} > 0, C_{33} > 0, C_{44} > 0, C_{55} > 0, C_{66} > 0, [C_{11} + C_{22} + C_{33} \\ &+ 2(C_{12} + C_{13} + C_{23})] > 0, (C_{11} + C_{22} - 2C_{12}) \\ &> 0, (C_{11} + C_{33} - 2C_{13}) > 0, (C_{22} + C_{33} - 2C_{23}) > 0. \end{aligned} \quad (3)$$

For the intermediate members with a monoclinic crystal structure, the mechanical stability was assessed using the corresponding mechanical stability criteria for monoclinic systems.

$$\begin{aligned} &C_{11} > 0, C_{22} > 0, C_{33} > 0, C_{44} > 0, C_{55} > 0, C_{66} > 0, [C_{11} + C_{22} \\ &+ C_{33} + 2(C_{12} + C_{13} + C_{23})] > 0, (C_{33}C_{55} - C_{13}^2) \\ &> 0, (C_{44}C_{66} - C_{24}^2) > 0, (C_{22} + C_{33} - 2C_{23}) > 0. \end{aligned} \quad (4)$$

The electronic band gaps of solid state semiconductor materials are typically underestimated by the GGA exchange-correlation functional [52]. Therefore, to achieve more accurate band gap predictions, we implemented the Heyd-Scuseria-Ernzerhof (HSE06) hybrid functional [53,54], which incorporates 25 % exact exchange from Hartree-Fock theory and 75 % exchange-correlation from the GGA functional. In the context of semiconductors and insulators, the HSE06 hybrid functional has demonstrated greater accuracy in predicting experimental results compared to standard GGA functionals.

Using the GGA functional, we computed the electronic density of states (DOS) and band structure, while the frequency-dependent complex dielectric function ($\varepsilon_1 + i\varepsilon_2$) for $Sb_2(S_xSe_{1-x})_3$ alloys was calculated using HSE06 functional [55]. The absorption coefficient (α) and the reflectivity (r) [56–58] were derived as:

$$\alpha = \frac{4\pi k}{\lambda} \text{ and } r = \frac{(n-1)^2 + k^2}{(n+1)^2 + k^2}, \text{respectively;} \quad (5)$$

where

$$\text{extinction coefficient, } k = \sqrt{\frac{\sqrt{\varepsilon_1^2 + \varepsilon_2^2} - \varepsilon_1}{2}}, \text{ refractive index, } n = \sqrt{\frac{\sqrt{\varepsilon_1^2 + \varepsilon_2^2} + \varepsilon_1}{2}}, \quad (6)$$

and λ is the wavelength of the photon [59,60].

The effective masses (m*) of holes ($m_h^* = m_h/m_o$) and electrons ($m_e^* = m_e/m_o$) were calculated from the band structure calculations using the sumo-bandstats scripts available in Sumo software [61], where m_h represents the mass of a hole in the lattice, m_e represents the mass of an electron in the lattice, and m_o is the electron rest mass.

To gain further insights into the chemical bonding, we performed crystal orbital Hamilton population (COHP) using the Local-Orbital Basis Suite Toward Electric-structure Reconstruction (LOBSTER) package [24,47,62–66]. Additionally, to analyze the charge transfer during the formation of the compound, we calculated the effective charges on each chemical species through Bader analysis [67–71]. To investigate the phonon behavior within the crystal, we used the Phonopy [72] package to compute the phonon density of states (DOS) for $Sb_2(S_xSe_{1-x})_3$ alloys.

3. Results

3.1. Structural and energetic properties

The end members: Sb_2Se_3 and Sb_2S_3, and the alloys of $Sb_2(S_xSe_{1-x})_3$ have been mostly studied experimentally in orthorhombic crystal structure [1,2,9,10,73,74]. In our study, we chose the SQS [28] approach, consisting of 20 atoms, to model the intermediate compositions of the $Sb_2(S_xSe_{1-x})_3$ alloys. This cell size provides a balance

between computational feasibility and accuracy, capturing overall trends without the artificial periodicity present in smaller cells, as supported by prior studies [75,76] on disordered systems. The lattice constants presented in Table 1 show a deviation from Vegard's law [77] and indicate a structural phase separation across the alloy system. A similar non-linear trend has been reported for the $GaSe_{1-x}Te_x$ and $Ga_{1-x}In_xSe$ alloys by Rak et al. [78], due to atomic size mismatch between dopants (In and Te) and host atoms, and a phase separation in the composition range $0.26 < x < 0.60$ in $GaSe_{1-x}Te_x$ from hexagonal (GaSe) to monoclinic (GaTe) [79]. In our alloy system, the end members exhibit an orthorhombic crystal structure (space group: *Pnma*), while the intermediate compositions adopt a monoclinic one (space group: *Pm*), characterized by lattice angles of 89.7°, 90°, and 90°.

Table 1 displays the equilibrium lattice constants and formation energies per formula unit for the $Sb_2(S_xSe_{1-x})_3$ alloy system, calculated using the GGA functional. No magnetic properties were observed for the $Sb_2(S_xSe_{1-x})_3$ alloys. Our computed lattice constants using the GGA functional closely align with the experimental results [1,73]. The formation energy of Sb_2Se_3 is significantly more negative (– 4.53 eV) compared to that of intermediate alloys and Sb_2S_3, which exhibit values around −1.23 to −1.24 eV. This trend indicates that the incorporation of sulfur (S) into Sb_2Se_3 reduces the stability of the resulting compounds. The observed changes in lattice constants and formation energies suggest that alloying with S induces a structural separation in the $Sb_2(S_xSe_{1-x})_3$ alloys.

3.2. Mechanical properties

Table S2 and Table S3 provide the values of the elastic and mechanical properties for the $Sb_2(S_xSe_{1-x})_3$ alloys, including elastic stiffness constants (C_{ij}), mechanical stability, bulk modulus (B), shear modulus (G), Pugh's ratio (κ), Vickers hardness (Hv), and Young's modulus (Y), calculated using the GGA functional. According to the criteria for mechanical stability [50], all members of the $Sb_2(S_xSe_{1-x})_3$ alloys are mechanically stable, except for the composition with $x = 0.25$. The values of the elastic tensors (C_{ij}) for $Sb_2(S_xSe_{1-x})_3$ do not exhibit any monotonic trend with respect to x, a pattern that is similarly reflected in the derived mechanical properties. The bulk modulus is similar across the intermediate compositions of $Sb_2(S_xSe_{1-x})_3$ alloy system, specifically at $x = 0.25$, $x = 0.50$, and $x = 0.75$. Moreover, lower formation energies (e.g., – 4.53 eV for Sb_2Se_3, Table 1) correspond to higher Vickers hardness values (e.g., 2.66 GPa, Table S3), indicating a balance between stability and mechanical strength. The calculated values of κ determine whether the material is ductile ($\kappa \leq 0.57$) or brittle ($\kappa > 0.57$) [46,80–83]. Our study shows that all compositions are ductile in nature and mechanically soft, as presented in Table S3. These values of mechanical properties serve as predictions for future experimental studies.

Table 1
Lattice constants of alloy $Sb_2(S_xSe_{1-x})_3$ along with their formation energies, calculated using the GGA functional. The formation energy is given per formula unit. Values from the literature are listed where available.

Material	Space Group	Lattice Constants (Å)			Formation Energy (eV)
		a	b	c	
Sb_2Se_3	*Pnma*	3.96, 3.98[a], 3.97[b]	11.21, 11.63[a], 11.64[b]	11.51, 11.78[a], 11.78[b]	−4.53
$Sb_2(S_{0.25}Se_{0.75})_3$	*Pm*	3.99	11.16	12.69	−1.23
$Sb_2(S_{0.50}Se_{0.50})_3$	*Pm*	3.95	11.35	12.60	−1.24
$Sb_2(S_{0.75}Se_{0.25})_3$	*Pm*	3.91	11.31	12.36	−1.24
Sb_2S_3	*Pnma*	3.87, 3.84[a], 3.84[b]	11.23, 11.23[a], 11.25[b]	12.13, 11.31[a], ,11.32[b]	−1.23

[a] Experimental Ref. [73].
[b] Experimental Ref. [1].

3.3. Vibrational properties

Fig. 1 displays the phonon total density of states (TDOS) for the members of the $Sb_2(S_xSe_{1-x})_3$ calculated using the GGA functional. All members are dynamically stable, as no phonon TDOS appears in the negative frequency region, which would indicate vibrational instability. The phonon TDOS for all compositions is distributed within the frequency range of approximately 0–10 THz. The end members ($x = 0.00$ and $x = 1.00$) exhibit relatively higher peak intensities compared to the intermediate compositions. As the composition varies from $x = 0.00$ to $x = 1.00$, both the peak positions and their intensities shift. However, for $x = 0.25$ and $x = 0.50$, the phonon TDOS patterns remain similar, suggesting consistent vibrational activity within this range. A gradual transition in vibrational properties is observed as S content increases. The overall TDOS remains stable and is verified experimentally. Phonon-phonon interactions at higher temperatures could facilitate experimental validation, as the current DFT calculations are conducted at 0 K [84]. To provide a more complete representation of the thermal properties of $Sb_2(S_xSe_{1-x})_3$ alloys, Table S6 is presented in the supplementary section.

3.4. Electronic properties

Fig. 2 illustrates the local density of states (LDOS) for $Sb_2(S_xSe_{1-x})_3$ alloys, computed using the GGA functional. The band gaps are presented in Table 2, which shows a linear increase from 1.06 eV to 1.78 eV as x increases from 0.00 to 1.00. Antimony (Sb) exhibits a relatively consistent LDOS across all concentrations (panels (a), (b), (c), (d), and (e)), with peaks appearing both below and above the Fermi level. As the S concentration increases, its contribution to the LDOS also rises, with S dominating at $x = 1.00$.

At $x = 0.25$ and $x = 0.50$, there is a noticeable transition where the contributions of S and Selenium (Se) become more balanced, with both elements showing peaks in similar energy ranges. As the concentration of S increases, the energy levels of the states shift. This shift is observable as the peaks in the LDOS plot move to different energy levels, indicating

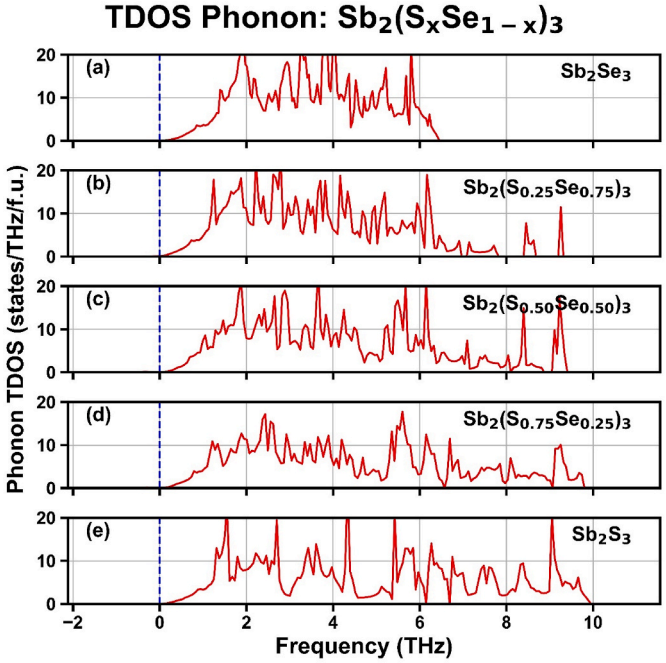

Fig. 1. Comparison of the phonon total density of states (TDOS) for vibrationally stable $Sb_2(S_xSe_{1-x})_3$ alloys at compositions $x = 0.00$, 0.25, 0.50, 0.75, and 1.00, shown in panels (a–e), respectively. The vertical dashed line at 0 THz indicates the zero-frequency reference.

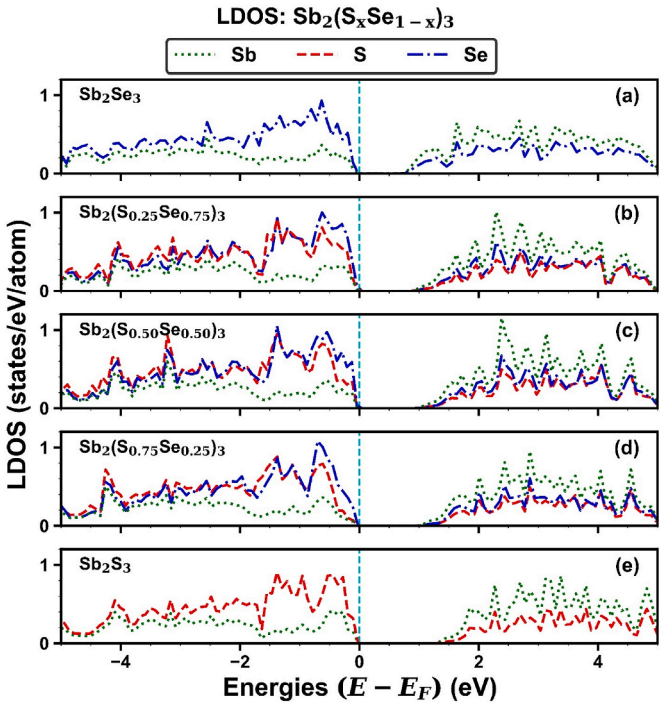

Fig. 2. Local density of states (LDOS) for the $Sb_2(S_xSe_{1-x})_3$ alloy system at concentrations x = 0.00, 0.25, 0.50, 0.75, and 1.00, presented in panels (a–e), respectively. The Fermi level is set at 0 eV.

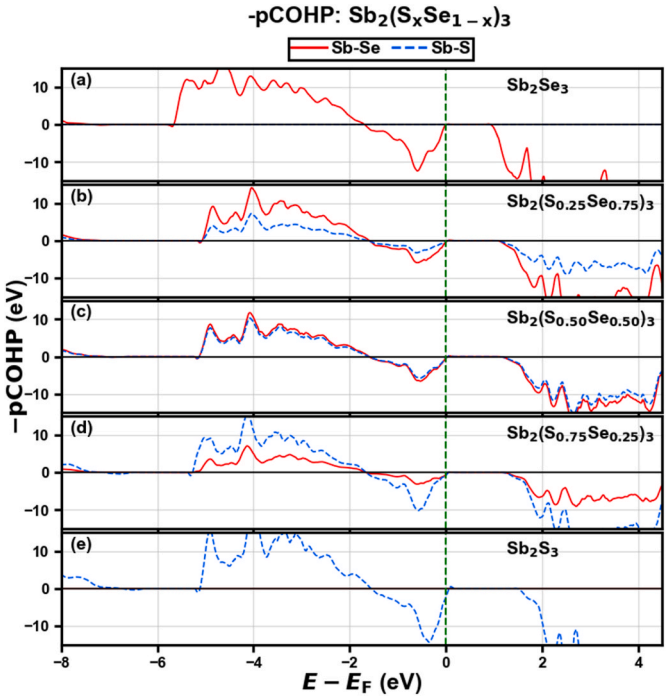

Fig. 3. The negative projected Crystal Orbital Hamilton Populations (-pCOHP) as a function of energy for alloys $Sb_2(S_xSe_{1-x})_3$ at different concentrations (x = 0.00, 0.25, 0.50, 0.75, and 1.00), presented in panels (a, b, c, d, e), respectively. Positive and negative values of -pCOHP correspond to bonding and antibonding interactions respectively. The Fermi level is set at 0 eV.

Table 2
Bandgaps of $Sb_2(S_xSe_{1-x})_3$ calculated using the GGA and HSE06 functional. Values from the literature are listed where available.

Material	Space Group	Bandgap (eV), Indirect	
		GGA	HSE06
Sb_2Se_3	*Pnma*	1.06, 1.1[a], 1.1[b], 1.1[c], 1.06[d], 1.1[e]	1.39
$Sb_2(S_{0.25}Se_{0.75})_3$	*Pm*	1.24	1.43
$Sb_2(S_{0.50}Se_{0.50})_3$	*Pm*	1.32	1.49
$Sb_2(S_{0.75}Se_{0.25})_3$	*Pm*	1.40	1.56
Sb_2S_3	*Pnma*	1.78, 1.8[a], 1.7[b], 1.7[c], 1.88[e],1.74[f]	1.89

[a] Experimental Ref. [10].
[b] Experimental Ref. [2].
[c] Experimental Ref. [9].
[d] Theoretical Ref. [95].
[e] Experimental Ref. [74].
[f] Experimental Ref. [96].

changes in the material's electronic structure. These variations in LDOS with different concentrations suggest that the electronic properties can be tuned by adjusting the S to Se ratio. This tunability is crucial for optimizing the material for specific electronic or optoelectronic applications.

To further elucidate these results, we have computed the bonding information using the crystal orbital Hamilton population (COHP) method, which is effective for analyzing bonding. Interactions based on wave functions or electron densities [63,85]. Specifically, we calculated the negative of the projected COHP (-pCOHP) using GGA, as shown in Fig. 3. In the -pCOHP analysis, a positive value indicates bonding interactions, a negative value indicates antibonding interactions, and a value of zero corresponds to non-bonding interactions. These calculations account for all interactions between nearest neighbors. For Sb-Se interactions (red lines), bonding states dominate at lower sulfur concentrations (x = 0.00 and 0.25), with notable bonding peaks below the valence band maximum (VBM). As energy increases, antibonding states become more prominent. For Sb-S interactions (blue lines), bonding states increase with rising sulfur concentration, with significant bonding peaks observed at x > 0.25. At x = 0.50, there is a balance between Sb-Se and Sb-S interactions, with noticeable contributions from both. At higher S concentrations (x = 0.75 and 1.00), Sb-S interactions clearly dominate, indicating that S substitution significantly alters the alloy's bonding characteristics. The shifting -pCOHP peaks suggest that the electronic structure and bonding characteristics of $Sb_2(S_xSe_{1-x})_3$ can be tuned by varying the S concentration, highlighting the potential for optimizing the materials properties for specific applications.

The integration of the crystal orbital Hamilton population (iCOHP) up to the Fermi level gives an indication of the bond strength between two atoms. A higher value indicates weaker bond strength and vice versa. The iCOHP values, in eV, are −1.16, −1.34, −1.22, −1.24 and −1.25 for x = 0.00, 0.25, 0.50, 0.75, and 1.00 respectively. The highest value is observed for pure Sb_2Se_3 (x = 0.00), and as x increases, the iCOHP becomes almost constant for x = 0.50, 0.75, and 1.00. This trend is further supported by the formation energy values in Table 1. Therefore, both the iCOHP values and formation energy exhibit a similar trend with increasing x, except for x = 0.00 and x = 0.25.

Table S1 shows the charge distribution for Sb, S, and Se in various compositions of the $Sb_2(S_xSe_{1-x})_3$ alloy system. The values are derived from Bader charge partitioning analysis using the GGA functional. We define charge transfer as the amount of negative charge, in terms of elementary electronic charge (-e). The results show that charge transfer varies across the alloys. The magnitude of this variation is largely dependent on the compound. Both S and Se display a consistently narrow range of charge transfer values across all compositions of the alloy, while Sb shows slight variations ranging from 0.88 e in Sb_2Se_3 to 1.18 e in Sb_2S_3 as x varies in the alloy. The electronegativities of Sb, S, and Se are 1.82 e, 2.44 e, and 2.48 e respectively, based on electrostatic force calculated by Allred et al. [86], which explains the observed charge transfer trends and bonding behavior. The range of charge transfer is directly related to variations in bond lengths and angles. Therefore, we conclude that the charge transfer and crystal structure are closely linked.

To further characterize the electronic properties of the alloys, we examine the electronic band structure. The band gap values for intermediate compositions were computed using the SQS [28] approach and were found to deviate from Vegard's law, resulting in band gap bowing. This deviation arises from the incorporation of sulfur, which induces local structural distortions and bonding asymmetry during alloying. Sandu et al. [87] applied SQS-generated structures to study the $ZnTe_{x}Se_{1-x}$ alloy system and reported excellent agreement between SQS-based predictions and experimental bowing parameters. The calculated band gaps compared to experimental data are listed in Table 2. All band gap values are indirect in nature. The results show that the GGA approximation provides a reasonable estimate for $Sb_2(S_xSe_{1-x})_3$, comparing well with experimental values for end members [8–12]. It also shows a small deviation from the hybrid HSE06 functional. Fig. 4 displays the calculated band gaps. We observe that there is a linear trend in the band gap (y) for this alloy system as the concentration (x) increases. The equation for the best-fit linear plot is given by:

$$y = (0.6388\,x + 1.0399)\ \text{eV}.$$

Table S4 provides both average electron and hole effective masses across all five members of the $Sb_2(S_xSe_{1-x})_3$ alloy system, calculated along different k-points paths. Fig. 5 illustrates these effective masses. Both electron and hole effective masses exhibit non-linear behavior with respect to sulfur concentration, indicating complex interactions within the material's electronic structure as the composition changes. The presence of peaks and troughs suggests that there are optimal compositions for minimizing or maximizing the effective mass, which could be crucial for tuning the electronic properties for specific applications. The effective mass for electrons reaches a minimum around $x \approx 0.15$, while for holes, the minimum occurs around $x \approx 0.25$, and increases towards the end members. Understanding these trends is essential for the design of optoelectronic devices, where effective mass plays a significant role in determining carrier mobility and, consequently, the performance of devices such as solar cells and photodetectors.

The electronic band structure for all five members of the $Sb_2(S_xSe_{1-x})_3$ alloy system, calculated along high-symmetry lines, is shown in Fig. 6. Each panel (a, b, c, d, e) represents the band structure for a

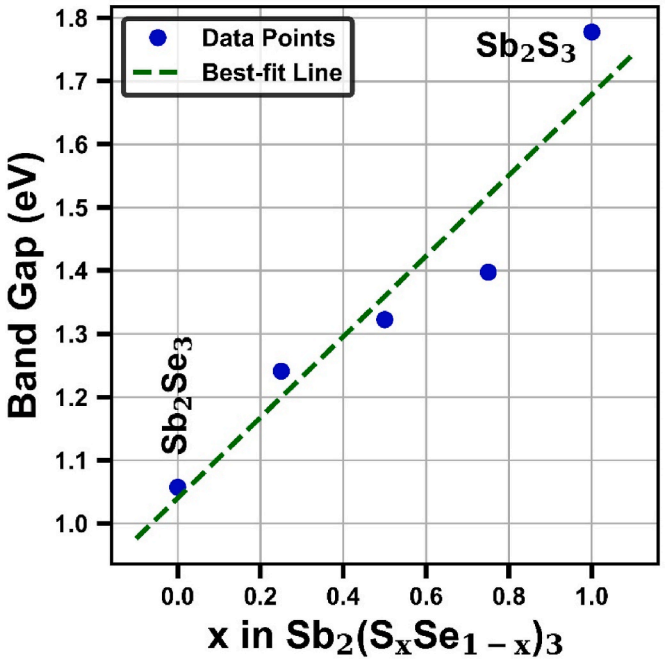

Fig. 4. Variation of the band gap (GGA) with compositions (x) in $Sb_2(S_xSe_{1-x})_3$ alloys. Blue dots indicate the calculated data points, and the green dashed line represents the best-fit linear trend.

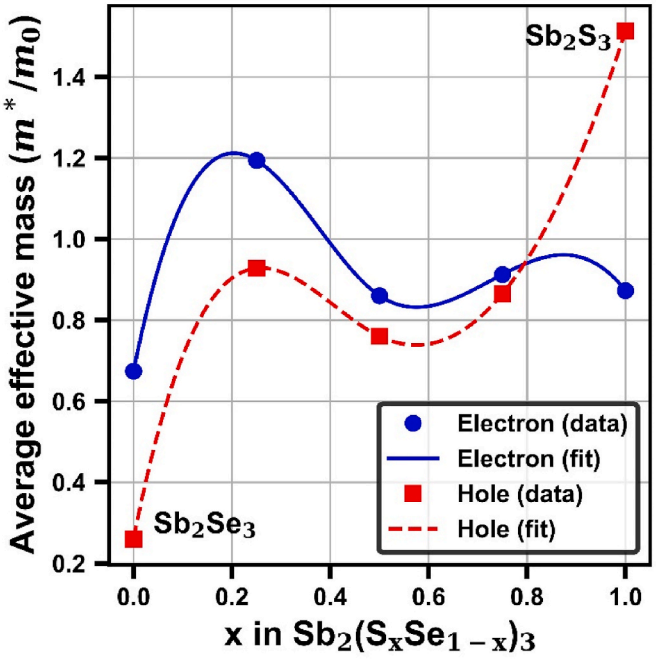

Fig. 5. Effective carrier masses for concentrations (x) in $Sb_2(S_xSe_{1-x})_3$ alloys. Electron effective masses (blue cubic spline curve) and hole effective masses (red cubic spline curve) are normalized to m_0 – the electron rest mass. Blue circles and red squares represent the data points, calculated as the arithmetic mean of the electron and hole masses, respectively.

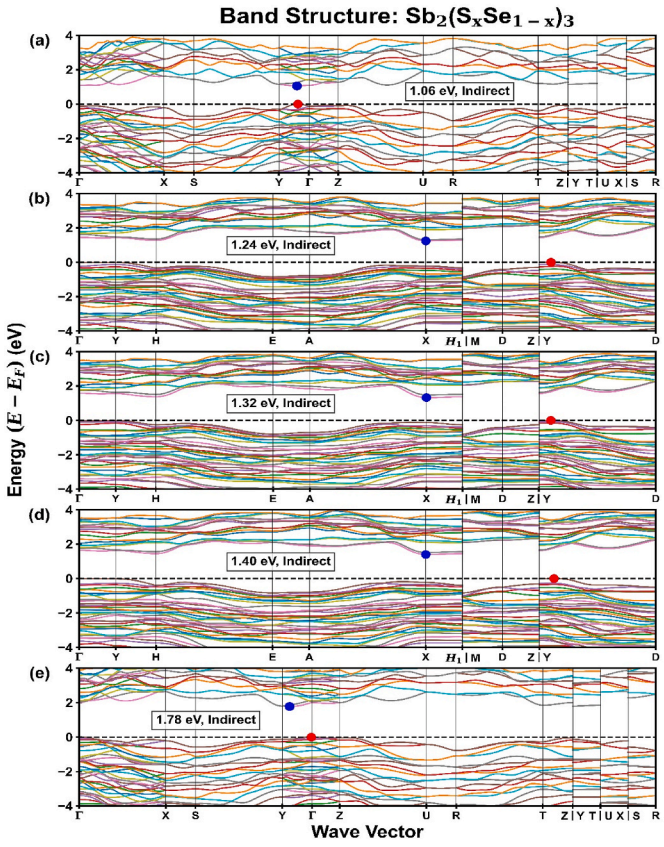

Fig. 6. The electronic band structures for the alloys $Sb_2(S_xSe_{1-x})_3$ at the concentrations (x = 0.00, 0.25, 0.50, 0.75, and 1.00), presented in panels (a, b, c, d, e) respectively. The red and blue dots mark the valence band maximum (VBM) and conduction band minimum (CBM), respectively.

different alloy composition. The fundamental band gap was calculated using the GGA functional for different concentrations (x = 0.00, 0.25, 0.50, 0.75, and 1.00). Table S5 displays the valence band maximum (VBM), conduction band minimum (CBM), band gaps, and their respective k-point locations. For the end members, the band gap occurs between the paths from Γ to Y. The smallest value is 1.06 eV for Sb_2Se_3, and the highest is 1.78 eV for Sb_2S_3. The intermediate values lie between these limits. Hence, the band gap of $Sb_2(S_xSe_{1-x})_3$ can be tuned within the range of 1.1–1.7 eV.

3.5. Optical properties

Fig. 7 displays the plots of absorption coefficient and reflectivity versus photon energy in the range of 0–3.5 eV, for all five members of the $Sb_2(S_xSe_{1-x})_3$ alloy system. For comparison, the spectral irradiance of the Air Mass 1.5 Global solar spectrum is also plotted alongside the absorption coefficient and reflectivity [88]. The absorption coefficient increases with photon energy for all members, showing a significant rise in the visible region beginning near the band gaps. The calculated absorption onset for the alloy system lies within the optimal range of 1.2–1.5 eV, comparable to the bandgap of CdTe (~1.48 eV) [89,90]. The absorption coefficients, on the order of 10^5 cm^{-1} near the absorption edge, are like those of CdTe and CIGS, suggests that thin-film absorber layers are feasible [35,91–93]. Furthermore, in more complex alloys, DFT studies on novel Sr_2UXO_6 (X = Mn, Zn) double perovskites also demonstrated strong optoelectronic potential due to their high absorption capabilities [94].

The reflectivity of $Sb_2(S_xSe_{1-x})_3$ exhibits a clear dependence on the sulfur content (x) across the 0–3.5 eV photon energy range. As x increases from 0 (Sb_2Se_3) to 1 (Sb_2S_3), the reflectivity generally decreases, particularly noticeable at lower energy values (0–1.5 eV). For x = 0, it is highest across the entire energy range, while for x = 1, it is lowest and increases more gradually with energy. The intermediate compositions (x = 0.25, 0.50, 0.75) exhibit values between those of the end members (x = 0.00 and x = 1.00). Hence, given its absorption coefficient and reflectivity, this alloy system is a suitable candidate for the absorber layer in solar cells. To provide a more complete representation of the optical properties, the complex dielectric function and refractive index are presented as Fig. S4 and S5 in the Supplementary section.

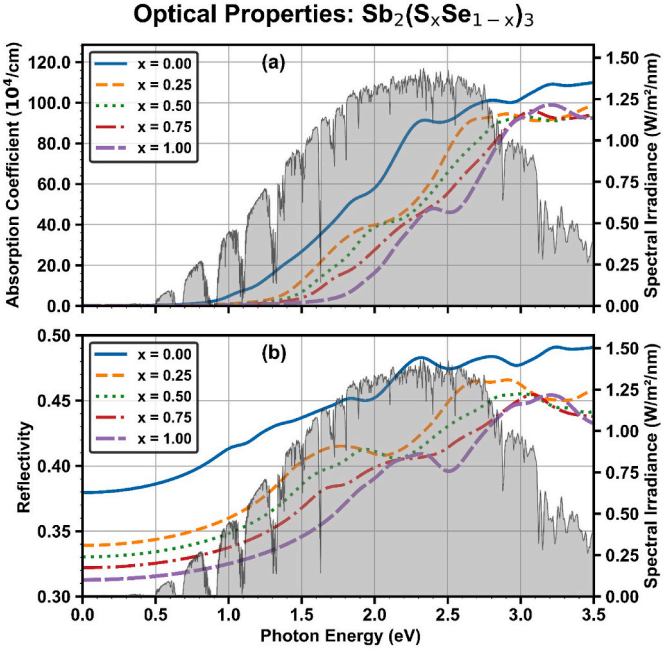

Fig. 7. (a) Absorption coefficient (α) and (b) reflectivity for $Sb_2(S_xSe_{1-x})_3$ alloys at concentrations of x = 0.00, 0.25, 0.50, 0.75, and 1.00, corresponding to the left-hand axes. They overlay the AM 1.5G spectral irradiance [88], shown in gray, of which the scales are on the right-hand axes. (For interpretation of the references to color in this figure legend, the reader is referred to the web version of this article.)

4. Conclusion

We have computationally studied the structural, energetic, mechanical, vibrational, electronic, and optical properties of the $Sb_2(S_xSe_{1-x})_3$ alloy system utilizing DFT and beyond. Most of our results are predictive in nature, as there is no experimental work on the intermediate members of this alloy system. We observed variations in lattice constants and formation energies across all alloy members of $Sb_2(S_xSe_{1-x})_3$ (for x = 0.00, 0.25, 0.50, 0.75, and 1.00). The end members exhibit an orthorhombic crystal system, while the intermediate compositions display monoclinic symmetry. The intermediate alloys have similar bulk modulus (B) values. Except for x = 0.25, all members of this alloy system are mechanically stable. Furthermore, all members of this alloy system are vibrationally stable. The band gap increases linearly with increasing sulfur concentration. The average electron effective masses are an order of magnitude higher than the hole effective masses, except for x = 1.00. Moreover, the alloy system's high absorption coefficient, low reflectivity, and optimal band gap range make all five members ideal for solar cell applications.

CRediT authorship contribution statement

M. Sitaula: Writing – review & editing, Writing – original draft, Visualization, Validation, Software, Methodology, Investigation. **V.T. Barone:** Writing – review & editing, Software, Methodology. **S.R. Kandel:** Software, Methodology. **B. K C:** Writing – review & editing, Software, Methodology. **B.B. Dumre:** Conceptualization. **R.J. Ellingson:** Project administration, Funding acquisition, Conceptualization. **S. V. Khare:** Writing – review & editing, Writing – original draft, Supervision, Resources, Project administration, Funding acquisition, Conceptualization.

Disclaimer

The views and conclusions contained herein are those of authors and should not be interpreted as necessarily representing the official policies or endorsements, either expressed or implied, of Air Force Research Laboratory or the U.S. Government.

Declaration of competing interest

The authors declare that they have no known competing financial interests or personal relationships that could have appeared to influence the work reported in this paper.

Acknowledgements

This material is based on research sponsored by the Air Force Research Laboratory (AFRL) under Agreement No. FA9453-19-C-1002. The U.S. Government is authorized to reproduce and distribute reprints for Governmental purposes not withstanding any copyright notation thereon. The views expressed are those of the authors and do not reflect the official guidance or position of the United States Government, the Department of Defense or of the United States Air Force. The appearance of external hyperlinks does not constitute endorsement by the United States Department of Defense (DoD) of the linked websites, or the information, products, or services contained therein. The Dod does not exercise any editorial, security, or other control over the information you may find at these locations. Approved for public release; distribution is unlimited. Public Affairs release approval Grant No. AFRL-2025-0688.

The calculations for this research were conducted at the University of Toledo computing clusters.

Appendix A. Supplementary data

Supplementary data to this article can be found online at https://doi.org/10.1016/j.cocom.2025.e01103.

Data availability

Data will be made available on request.

References

[1] E.A. Rueda Pérez, E. Regalado-Pérez, A. Cerdán-Pasarán, R.G. Avilez García, N. R. Mathews, $Sb_2(S_xSe_{1-x})_3$ thin films by electrodeposition: role of deposition potential on the formation of the solid solution and photovoltaic performance via device simulation current, Appl. Phys. 47 (2023) 44–53, https://doi.org/10.1016/j.cap.2022.12.011.

[2] X. Wang, R. Tang, C. Wu, C. Zhu, T. Chen, Development of antimony sulfide–selenide $Sb_2(S,Se)_3$-based solar cells, J. Energy Chem. 27 (2018) 713–721, https://doi.org/10.1016/j.jechem.2017.09.031.

[3] F. Gao, X. Li, X. Xiong, K. Li, Y. Xie, J. Luo, B. Li, G. Zeng, M. Ghali, Preparation and characterization of $Sb_2(S_xSe_{1-x})_3$ thin films deposited by pulsed laser deposition, J. Mater. Sci. Mater. Electron. 33 (2022) 26086–26099, https://doi.org/10.1007/s10854-022-09296-1.

[4] A. Hernández-Granados, J. Escorcia-García, D. Peréz-Martínez, J. García-Cerrillo, C. Menchaca-Campos, H. Hu, $Sb_2(S_xSe_{1-x})_3$ sensitized solar cells prepared by solution deposition methods, Mater. Sci. Semicond. Process. 56 (2016) 222–227, https://doi.org/10.1016/j.mssp.2016.08.022.

[5] T.D. Lee, A.U. Ebong, A review of thin film solar cell technologies and challenges, Renew. Sustain. Energy Rev. 70 (2017) 1286–1297, https://doi.org/10.1016/j.rser.2016.12.028.

[6] Z. Li, H. Zhu, Y. Guo, X. Niu, X. Chen, C. Zhang, W. Zhang, X. Liang, D. Zhou, J. Chen, Y. Mai, Efficiency enhancement of Sb_2Se_3 thin-film solar cells by the co-evaporation of Se and Sb_2Se3, APEX 9 (2016) 052302, https://doi.org/10.7567/apex.9.052302.

[7] Y. Pan, X. Hu, Y. Guo, X. Pan, F. Zhao, G. Weng, J. Tao, C. Zhao, J. Jiang, S. Chen, P. Yang, J. Chu, Vapor transport deposition of highly efficient $Sb_2(S,Se)_3$ solar cells via controllable orientation growth, Adv. Funct. Mater. 31 (2021) 2101476, https://doi.org/10.1002/adfm.202101476.

[8] A. Adhikari, S. Rijal, M.K. Jamarkattel, S. Neupane, J. Blodgett, D. Pokhrel, T. Zhu, V. Karade, M.J. Heben, R.J. Ellingson, Process optimization and light soaking to enhance photovoltaic performance of antimony sulfide solar cells, ACS Appl. Energy Mater. (2025), https://doi.org/10.1021/acsaem.4c03160.

[9] Y. Lu, K. Li, X. Yang, S. Lu, S. Li, J. Zheng, L. Fu, C. Chen, J. Tang, HTL-free $Sb_2(S,Se)_3$ solar cells with an optimal detailed balance band gap, ACS Appl. Mater. Interfaces 13 (2021) 46858–46865, https://doi.org/10.1021/acsami.1c10758.

[10] F. De Bray Sánchez, M.T.S. Nair, P.K. Nair, Optimum chemical composition of antimony sulfide selenide for thin film solar cells, Appl. Surf. Sci. 454 (2018) 305–312, https://doi.org/10.1016/j.apsusc.2018.05.076.

[11] S. Rühle, Tabulated values of the shockley–queisser limit for single junction solar cells, Sol. Energy 130 (2016) 139–147, https://doi.org/10.1016/j.solener.2016.02.015.

[12] Y. Xiao, L. Feng, H. Wang, A CTL-Free homo-heterojunction antimony chalcogenide solar cell: theoretical study, J. Phys. Chem. Solid. 184 (2024) 111742, https://doi.org/10.1016/j.jpcs.2023.111742.

[13] J.F.G. Kresse, Efficiency of ab-initio total energy calculations for metals and semiconductors using a plane-wave basis set, Comput. Mater. Sci. 6 (1996) 15–50, https://doi.org/10.1016/0927-0256(96)00008-0.

[14] J.F.G. Kresse, Efficient iterative schemes for ab initio total-energy calculations using a plane-wave basis set, Phys. Rev. B 54 (1996) 11169–11186, https://doi.org/10.1103/PhysRevB.54.11169.

[15] G. Kresse, J. Hafner, Ab initio molecular dynamics for liquid metals, Phys. Rev. B Condens. Matter 47 (1993) 558–561, https://doi.org/10.1103/physrevb.47.558.

[16] D.J.G. Kresse, From ultrasoft pseudopotentials to the projector augmented-wave method, Phys. Rev. B 59 (1999) 1758–1775, https://doi.org/10.1103/PhysRevB.59.1758.

[17] N. Jiang, J.L. Roehl, S.V. Khare, D.G. Georgiev, A.H. Jayatissa, An ab initio computational study of pure Zn_3N_2 and its native point defects and dopants Cu, Ag and Au, Thin Solid Films 564 (2014) 331–338, https://doi.org/10.1016/j.tsf.2014.05.032.

[18] J. Roehl, S. Khare, Diffusion of Cd vacancy and interstitials of Cd, Cu, Ag, Au and Mo in CdTe: a first principles investigation, Sol. Energy 101 (2014) 245–253, https://doi.org/10.1016/j.solener.2013.12.017.

[19] J.P. Perdew, J.A. Chevary, S.H. Vosko, K.A. Jackson, M.R. Pederson, D.J. Singh, C. Fiolhais, Erratum: atoms, molecules, solids, and surfaces: applications of the generalized gradient approximation for exchange and correlation, Phys. Rev. B Condens. Matter 48 (1993) 4978, https://doi.org/10.1103/physrevb.48.4978.2.

[20] J.P. Perdew, J.A. Chevary, S.H. Vosko, K.A. Jackson, M.R. Pederson, D.J. Singh, C. Fiolhais, Atoms, molecules, solids, and surfaces: applications of the generalized gradient approximation for exchange and correlation, Phys. Rev. B Condens. Matter 46 (1992) 6671–6687, https://doi.org/10.1103/physrevb.46.6671.

[21] Y. Wang, Z.T. Liu, S.V. Khare, S.A. Collins, J. Zhang, L. Wang, Y. Zhao, Thermal equation of state of silicon carbide, Appl. Phys. Lett. 108 (2016), https://doi.org/10.1063/1.4941797.

[22] P.E. Blochl, Projector augmented-wave method, Phys. Rev. B Condens. Matter 50 (1994) 17953–17979, https://doi.org/10.1103/physrevb.50.17953.

[23] K. Zhang, K. Balasubramanian, B. Ozsdolay, C. Mulligan, S. Khare, W. Zheng, D. Gall, Epitaxial NbC_xN_{1-x} (001) layers: growth, mechanical properties, and electrical resistivity, Surf. Coating. Technol. 277 (2015) 136–143, https://doi.org/10.1016/j.surfcoat.2015.07.025.

[24] N.J. Szymanski, I. Khatri, J.G. Amar, D. Gall, S.V. Khare, Unconventional superconductivity in 3d rocksalt transition metal carbides, J. Mater. Chem. C 7 (2019) 12619–12632, https://doi.org/10.1039/c9tc03793d.

[25] K. Zhang, K. Balasubramanian, B. Ozsdolay, C. Mulligan, S. Khare, W. Zheng, D. Gall, Epitaxial NbC_xN_{1-x}(001) layers: growth, mechanical properties, and electrical resistivity, Surf. Coating. Technol. 277 (2015) 136–143, https://doi.org/10.1016/j.surfcoat.2015.07.025.

[26] I. Efthimiopoulos, I. Khatri, Z.T. Liu, S.V. Khare, P. Sarin, V. Tsurkan, A. Loidl, D. Zhang, Y. Wang, Universal link of magnetic exchange and structural behavior under pressure in chromium spinels, Phys. Rev. B 97 (2018) 184435, https://doi.org/10.1103/PhysRevB.97.184435.

[27] A. Jain, S.P. Ong, G. Hautier, W. Chen, W.D. Richards, S. Dacek, S. Cholia, D. Gunter, D. Skinner, G. Ceder, K.A. Persson, Commentary: the materials project: a materials genome approach to accelerating materials innovation, APL Mater. 1 (2013) 011002, https://doi.org/10.1063/1.4812323.

[28] A. Zunger, S. Wei, L.G. Ferreira, J.E. Bernard, Special quasirandom structures, Phys. Rev. Lett. 65 (1990) 353–356, https://doi.org/10.1103/PhysRevLett.65.353.

[29] N. Szymanski, V. Adhikari, M. Willard, P. Sarin, D. Gall, S. Khare, Prediction of improved magnetization and stability in $Fe_{16}N_2$ through alloying, J. Appl. Phys. 126 (2019), https://doi.org/10.1063/1.5109571.

[30] A. van de Walle, Multicomponent multisublattice alloys, nonconfigurational entropy and other additions to the alloy theoretic automated toolkit, Calphad 33 (2009) 266–278, https://doi.org/10.1016/j.calphad.2008.12.005.

[31] M.A. Axel van de Walle, G. Ceder, The Alloy-Theoretic Automated Toolkit (ATAT): a User Guide, 26, Dec. 2002, pp. 539–553, https://doi.org/10.1016/S0364-5916(02)80006-2.

[32] A. van de Walle, P. Tiwary, M. de Jong, D.L. Olmsted, M. Asta, A. Dick, D. Shin, Y. Wang, L.Q. Chen, Z.K. Liu, Efficient stochastic generation of special quasirandom structures, Calphad 42 (2013) 13–18, https://doi.org/10.1016/j.calphad.2013.06.006.

[33] B. Dumre, N. Szymanski, V. Adhikari, I. Khatri, D. Gall, S. Khare, Improved optoelectronic properties in $CdSe_xTe_{1-x}$ through controlled composition and short-range order, Sol. Energy 194 (2019) 742–750, https://doi.org/10.1016/j.solener.2019.10.091.

[34] S.R. Kandel, B.B. Dumre, D. Gall, S.V. Khare, Prediction of super hardness in transition metal hexa-nitrides from density functional theory computations, Materialia 25 (2022) 101550, https://doi.org/10.1016/j.mtla.2022.101550.

[35] B. Dumre, D. Gall, S. Khare, Stability, and electronic and optical properties of ternary nitride phases of $MgSnN_2$: a first-principles study, J. Phys. Chem. Solid. 153 (2021) 110011, https://doi.org/10.1016/j.jpcs.2021.110011.

[36] N.J. Szymanski, L.N. Walters, O. Hellman, D. Gall, S.V. Khare, Dynamical stabilization in delafossite nitrides for solar energy conversion, J. Mater. Chem. A 6 (2018) 20852–20860, https://doi.org/10.1039/c8ta07536k.

[37] R. Hill, The elastic behaviour of a crystalline aggregate, Proc. Phys. Soc. 65 (1952) 349–354, https://doi.org/10.1088/0370-1298/65/5/307.

[38] R.S. Anupama Upadhyay, Use of artificial neural network and theoretical modeling to predict the effective elastic modulus of composites with ellipsoidal inclusions, J. Appl. Math. Mech. 1 (2014) 1100903, https://doi.org/10.1002/zamm.19290090104.

[39] X. Zhou, D. Gall, S.V. Khare, Mechanical properties and electronic structure of anti-ReO_3 structured cubic nitrides, M_3N, of d block transition metals M: an ab initio study, J. Alloys Compd. 595 (2014) 80–86, https://doi.org/10.1016/j.jallcom.2014.01.116.

[40] B.B. Dumre, S.V. Khare, Interrelationship of bonding strength with structural stability of ternary oxide phases of $MgSnO_3$: a first-principles study, Phys. B Condens. Matter 637 (2022) 413896, https://doi.org/10.1016/j.physb.2022.413896.

[41] S.R. Kandel, B.B. Dumre, D. Gall, S.V. Khare, Investigation of hardness in transition metal hexa-nitrides in cubic structure: a first-principles study, J. Phys. Chem. Solid. 171 (2022) 111022, https://doi.org/10.1016/j.jpcs.2022.111022.

[42] P. Gunaicha, S. Gangam, J. Roehl, S. Khare, Structural, energetic and elastic properties of $Cu_2ZnSn(S_xSe_{1-x})_4$ (x= 1, 0.75, 0.5, 0.25, 0) alloys from first-principles computations, Sol. Energy 102 (2014) 276–281, https://doi.org/10.1016/j.solener.2014.01.015.

[43] S.F. Pugh, XCII. Relations between the elastic moduli and the plastic properties of polycrystalline pure metals, London, Edinburgh Dublin Phil. Mag. J. Sci. 45 (2009) 823–843, https://doi.org/10.1080/14786440808520496.

[44] S.A. Khattak, S.M. Wabaidur, M.A. Islam, M. Husain, I. Ullah, S. Zulfiqar, G. Rooh, N. Rahman, M.S. Khan, G. Khan, First-principles structural, elastic and optoelectronics study of sodium niobate and tantalate perovskites, Sci. Rep. 12 (2022) 21700, https://doi.org/10.1038/s41598-022-26250-7.

[45] G. Benabdellah, D. Toufik, M. Mokhtari, M.S. Khan, A.M. Tawfeek, H. Ahmad, Investigating the electronic structure, elastic, magnetic, and thermoelectric nature of $NiV_XSc_{1-X}Sb$ quaternary half-Heusler alloys, Model. Simulat. Mater. Sci. Eng. 32 (2024) 025002.

[46] Y. Tian, B. Xu, Z. Zhao, Microscopic theory of hardness and design of novel superhard crystals, Int. J. Refract. Metals Hard Mater. 33 (2012) 93–106, https://doi.org/10.1016/j.ijrmhm.2012.02.021.

[47] Z.T.Y. Liu, D. Gall, S.V. Khare, Electronic and bonding analysis of hardness in pyrite-type transition-metal pernitrides, Phys. Rev. B 90 (2014) 134102, https://doi.org/10.1103/PhysRevB.90.134102.

[48] Z.T.Y. Liu, X. Zhou, D. Gall, S.V. Khare, First-principles investigation of the structural, mechanical and electronic properties of the NbO-structured 3d, 4d and 5d transition metal nitrides, Comput. Mater. Sci. 84 (2014) 365–373, https://doi.org/10.1016/j.commatsci.2013.12.038.

[49] Z.T. Liu, X. Zhou, S.V. Khare, D. Gall, Structural, mechanical and electronic properties of 3d transition metal nitrides in cubic zincblende, rocksalt and cesium chloride structures: a first-principles investigation, J. Phys. Condens. Matter 26 (2014) 025404, https://doi.org/10.1088/0953-8984/26/2/025404.

[50] Z.-j. Wu, E.-j. Zhao, H.-p. Xiang, X.-f. Hao, X.-j. Liu, J. Meng, Crystal structures and elastic properties of superhard IrN_2 and IrN_3 from first principles, Phys. Rev. B 76 (2007) 054115, https://doi.org/10.1103/PhysRevB.76.054115.

[51] S.R. Kandel, B.B. Dumre, D. Gall, S.V. Khare, Mechanical and electronic properties of transition metal hexa-nitrides in hexagonal structure from density functional theory calculations, Comput. Mater. Sci. 221 (2023) 112084, https://doi.org/10.1016/j.commatsci.2023.112084.

[52] J. Paier, M. Marsman, K. Hummer, G. Kresse, I.C. Gerber, J.G. Angyan, Screened hybrid density functionals applied to solids, J. Chem. Phys. 124 (2006) 154709, https://doi.org/10.1063/1.2187006.

[53] A.V. Krukau, O.A. Vydrov, A.F. Izmaylov, G.E. Scuseria, Influence of the exchange screening parameter on the performance of screened hybrid functionals, J. Chem. Phys. 125 (2006) 224106, https://doi.org/10.1063/1.2404663.

[54] M.S. Khan, B. Gul, G. Khan, S.A. Khattak, M. Ajaz, T. Khan, S. Zulfiqar, Exploring the exemplary electronic and optical nature in $NaInX_2$ (X= S, Se and Te) ternary type chalcogenides materials: a GGA+ U and hybrid functionals study, J. Solid State Chem. 307 (2022) 122853, https://doi.org/10.1016/j.jssc.2021.122853.

[55] M. Gajdoš, K. Hummer, G. Kresse, J. Furthmüller, F. Bechstedt, Linear optical properties in the projector-augmented wave methodology, Phys. Rev. B 73 (2006) 045112, https://doi.org/10.1103/PhysRevB.73.045112.

[56] C. Kittel, Introduction to Solid State Physics, John Wiley & Sons, Inc., New York, 2005.

[57] M.S. Khan, B. Gul, G. Benabdellah, B. Ahmad, M.D. Albaqami, S.M. Wabaidur, H. Ahmad, Tailoring the optoelectronic, thermoelectric, and thermodynamic properties of rare-earth quaternary chalcogenides: an inclusive first-principles study, Mater. Today Commun. 38 (2024) 107848, https://doi.org/10.1016/j.mtcomm.2023.107848.

[58] M.S. Khan, B. Gul, G. Benabdellah, B. Ahmad, M. Ouladsmane, H. Ahmad, Unveiling the electronic, optical, thermoelectric, and thermodynamic properties of novel $SrXCu_3Se_4$ (X= In, Tl) materials: a systematic DFT study, Chem. Phys. Lett. 835 (2024) 141012, https://doi.org/10.1016/j.cplett.2023.141012.

[59] B. Gul, M.S. Khan, M. Rahaman, G. Periyasami, H. Ahmad, Cu-based novel transition-metals chalcogenides for advanced optoelectronic and thermoelectric devices: first-principles study, Phys. Scri. 99 (2024) 025954, https://doi.org/10.1088/1402-4896/ad1c7c.

[60] M.S. Khan, B. Gul, B. Ahmad, A.M. Tighezza, H. Ahmad, Insight into the electronic, optical, and transport properties of novel $BaLaCuX_3$ (X= S, Se, and Te) quaternary chalcogenides, J. Solid State Chem. 330 (2024) 124496, https://doi.org/10.1016/j.jssc.2023.124496.

[61] A. Ganose, A.J. Jackson, Sumo 1.0.6: heavyweight plotting tools for ab initio solid-state calculations. https://pypi.org/project/sumo/1.0.6, 2018.

[62] S. Maintz, V.L. Deringer, A.L. Tchougreeff, R. Dronskowski, LOBSTER: a tool to extract chemical bonding from plane-wave based DFT, J. Comput. Chem. 37 (2016) 1030–1035, https://doi.org/10.1002/jcc.24300.

[63] V.L. Deringer, A.L. Tchougreeff, R. Dronskowski, Crystal orbital Hamilton population (COHP) analysis as projected from plane-wave basis sets, J. Phys. Chem. A 115 (2011) 5461, https://doi.org/10.1021/jp202489s.

[64] S. Maintz, V.L. Deringer, A.L. Tchougreeff, R. Dronskowski, Analytic projection from plane-wave and PAW wavefunctions and application to chemical-bonding analysis in solids, J. Comput. Chem. 34 (2013) 2557–2567, https://doi.org/10.1002/jcc.23424.

[65] S. Maintz, M. Esser, R. Dronskowski, Efficient rotation of local basis functions using real spherical harmonics, Acta Phys. Pol. B 47 (2016) 1165–1174, https://doi.org/10.5506/APhysPolB.47.1165.

[66] Z.T. Liu, B.P. Burton, S.V. Khare, D. Gall, First-principles phase diagram calculations for the rocksalt-structure quasibinary systems TiN-ZrN, TiN-HfN and ZrN-HfN, J. Phys. Condens. Matter 29 (2017) 035401, https://doi.org/10.1088/0953-8984/29/3/035401.

[67] G. Henkelman, A. Arnaldsson, H. Jónsson, A fast and robust algorithm for bader decomposition of charge density, Comput. Mater. Sci. 36 (2006) 354–360, https://doi.org/10.1016/j.commatsci.2005.04.010.

[68] E. Sanville, S.D. Kenny, R. Smith, G. Henkelman, Improved grid-based algorithm for bader charge allocation, J. Comput. Chem. 28 (2007) 899–908, https://doi.org/10.1002/jcc.20575.

[69] W. Tang, E. Sanville, G. Henkelman, A grid-based bader analysis algorithm without lattice bias, J. Phys. Condens. Matter 21 (2009) 084204, https://doi.org/10.1088/0953-8984/21/8/084204.

[70] M. Yu, D.R. Trinkle, Accurate and efficient algorithm for Bader charge integration, J. Chem. Phys. 134 (2011) 064111, https://doi.org/10.1063/1.3553716.

[71] S.R. Kandel, D. Gall, S.V. Khare, Density functional theory calculations of mechanical and electronic properties of $W_{1-x}Ta_xN_6$, $W_{1-x}Mo_xN_6$, and $Mo_{1-x}Ta_xN_6$ ($0 \leq x \leq 1$) alloys in hexagonal structure, J. Vac. Sci. Technol., A 41 (2023) 063112, https://doi.org/10.1116/6.0002923.

[72] A. Togo, I. Tanaka, First principles phonon calculations in materials science, Scr. Mater. 108 (2015) 1–5, https://doi.org/10.1016/j.scriptamat.2015.07.021.

[73] P.K. Nair, E.A. Zamudio Medina, G. Vázquez García, L. Guerrero Martínez, M.T. S. Nair, Functional prototype modules of antimony sulfide selenide thin film solar cells, Thin Solid Films 669 (2019) 410–418, https://doi.org/10.1016/j.tsf.2018.11.019.

[74] F. De Bray-Sánchez, M.T.S. Nair, P.K. Nair, Systematic variation of material characteristics with chemical composition in antimony sulfide selenide thin films and its relevance to solar cell performance, Phys. Status Solidi 218 (2021) 2000822, https://doi.org/10.1002/pssa.202000822.

[75] J. Xu, Y. Lu, Y. Shen, P. Li, Y. Zhang, A modified elastic constant calculation method for triclinic-like special quasi-random structures: application to Pd-M (M= Cu, Ag) solid solutions, Mater. Today Commun. 31 (2022) 103795, https://doi.org/10.1016/j.mtcomm.2022.103795.

[76] S. Chentouf, P. Maugis, Structural, energetic and dynamical properties of ordered and disordered bcc Fe25at.% Ni alloys: a first-principles study, Comput. Mater. Sci. 126 (2017) 82–89, https://doi.org/10.1016/j.commatsci.2016.09.020.

[77] A.R. Denton, N.W. Ashcroft, Vegard's law, Phys. Rev. 43 (1991) 3161, https://doi.org/10.1103/PhysRevA.43.3161.

[78] Z. Rak, S. Mahanti, K.C. Mandal, N. Fernelius, Doping dependence of electronic and mechanical properties of $GaSe_{1-x}Te_x$ and $Ga_{1-x}In_xSe$ from first principles, Phys. Rev. B Condens. Matter 82 (2010) 155203, https://doi.org/10.1103/PhysRevB.82.155203.

[79] F. Cerdeira, E. Meneses, A. Gouskov, Splittings and correlations between the long-wavelength optical phonons in the layer compounds GaSe, GaTe, and $GaSe_{1-x}Te_x$, Phys. Rev. B 16 (1977) 1648, https://doi.org/10.1103/PhysRevB.16.1648.

[80] X. Jiang, J. Zhao, X. Jiang, Correlation between hardness and elastic moduli of the covalent crystals, Comput. Mater. Sci. 50 (2011) 2287–2290, https://doi.org/10.1016/j.commatsci.2011.01.043.

[81] S. Pugh, XCII. Relations between the elastic moduli and the plastic properties of polycrystalline pure metals, London, Edinburgh Dublin Phil. Mag. J. Sci. 45 (1954) 823–843, https://doi.org/10.1080/14786440808520496.

[82] S. Kandel, B. Dumre, D. Gall, S. Khare, Investigation of hardness in transition metal hexa-nitrides in cubic structure: a first-principles study, J. Phys. Chem. Solid. 171 (2022) 111022, https://doi.org/10.1016/j.jpcs.2022.111022.

[83] B. Kc, V. Barone, S. Kandel, M. Sitaula, B. Dumre, R. Ellingson, S. Khare, Computational investigation of structural, electronic, and optical properties of $(In_xGa_{1-x})_2O_3$ alloys as candidates for emitter layer application in solar cells, Phys. B Condens. Matter (2025) 417615, https://doi.org/10.1016/j.physb.2025.417615.

[84] I. Khatri, N.J. Szymanski, B.B. Dumre, J.G. Amar, D. Gall, S.V. Khare, Correlating structure and orbital occupation with the stability and mechanical properties of 3d transition metal carbides, J. Alloys Compd. 891 (2022) 161866, https://doi.org/10.1016/j.jallcom.2021.161866.

[85] R.B. Dronskowski, P. E, Crystal Orbital Hamilton Populations (COHP). Energy-resolved visualization of chemical bonding in solids based on density-functional calculations, J. Phys. Chem. 97 (1993) 8617–8624, https://doi.org/10.1021/j100135a014.

[86] A.L. Allred, E.G. Rochow, A scale of electronegativity based on electrostatic force, J. Inorg. Nucl. Chem. 5 (1958) 264–268, https://doi.org/10.1016/0022-1902(58)80003-2.

[87] T. Sandu, R.I. Iftimie, Bandgaps and band bowing in semiconductor alloys, Solid State Commun. 150 (2010) 888–892, https://doi.org/10.1016/j.ssc.2010.01.046.

[88] C.A. Gueymard, The sun's total and spectral irradiance for solar energy applications and solar radiation models, Sol. Energy 76 (2004) 423–453, https://doi.org/10.1016/j.solener.2003.08.039.

[89] M.A. Green, Photovoltaics: technology overview, Energy Policy 28 (2000) 989–998, https://doi.org/10.1016/S0301-4215(00)00086-0.

[90] X. Wu, High-efficiency polycrystalline CdTe thin-film solar cells, Sol. Energy 77 (2004) 803–814, https://doi.org/10.1016/j.solener.2004.06.006.

[91] I. Repins, M.A. Contreras, B. Egaas, C. DeHart, J. Scharf, C.L. Perkins, B. To, R. Noufi, 19· 9%-efficient ZnO/CdS/CuInGaSe^2 solar cell with 81· 2% fill factor, Prog. Photovoltaics Res. Appl. 16 (2008) 235–239, https://doi.org/10.1002/pip.822.

[92] X. Wang, S.R. Kavanagh, D.O. Scanlon, A. Walsh, Upper efficiency limit of Sb_2Se_3 solar cells, Joule 8 (2024) 2105–2122, https://doi.org/10.1016/j.joule.2024.05.004.

[93] A. Mavlonov, T. Razykov, F. Raziq, J. Gan, J. Chantana, Y. Kawano, T. Nishimura, H. Wei, A. Zakutayev, T. Minemoto, A review of Sb_2Se_3 photovoltaic absorber materials and thin-film solar cells, Sol. Energy 201 (2020) 227–246, https://doi.org/10.1016/j.solener.2020.03.009.

[94] A. Ali, M.S. Khan, M. Irfan, G. Khan, B. Gul, S. Azam, H. Haider, A. Ullah, M. R. Karim, I.A. Alnaser, First-principles study of electronic, optical, magnetic, and thermoelectric properties of novel Sr_2UXO_6 (X= Mn, Zn) double perovskites, Chem. Phys. Lett. 835 (2024) 141019, https://doi.org/10.1016/j.cplett.2023.141019.

[95] L.-y. Lin, L.-q. Jiang, Y. Qiu, B.-d. Fan, Analysis of Sb_2Se_3/CdS based photovoltaic cell: a numerical simulation approach, J. Phys. Chem. Solid. 122 (2018) 19–24, https://doi.org/10.1016/j.jpcs.2018.05.045.

[96] H. Gao, J. Li, X. Peng, Y. Huang, Q. Zhao, H. Wang, T. Wu, S. Sheng, R. Tang, T. Chen, Band gap adjustable antimony selenosulfide indoor photovoltaics with 20% efficiency, Sol. RRL 8 (2024) 2400389, https://doi.org/10.1002/solr.202400389.